Numerical Heat Transfer, Part B, 45: 301–318, 2004

ISSN: 1040-7790 print/1521-0626 online
DOI: 10.1080/10407790490277931

Taylor & Francis
Taylor & Francis Group

A NEW WALL FUNCTION STRATEGY FOR COMPLEX TURBULENT FLOWS

T. J. Craft, S. E. Gant, H. Iacovides, and B. E. Launder
Department of Mechanical, Aerospace and Manufacturing Engineering, University of Manchester Institute of Science and Technology (UMIST), Manchester, United Kingdom

Wall functions are widely used and offer significant computational savings compared with low-Reynolds-number formulations. However, existing schemes are based on assumed near-wall profiles of velocity, turbulence parameters, and temperature which are inapplicable in complex, nonequilibrium flows. A new wall function has therefore been developed which solves boundary-layer-type transport equations across a locally defined subgrid. This approach has been applied to a plane channel flow, an axisymmetric impinging jet, and flow near a spinning disc using linear and nonlinear k–ε turbulence models. Computational costs are an order of magnitude less than low-Reynolds-number calculations, while a clear improvement is shown in reproducing low-Re predictions over standard wall functions.

1. INTRODUCTION

In most practical problems of convective heat transport to or from a rigid surface, the flow in the vicinity of the body is in turbulent motion. However, at the solid–fluid interface itself, the no-slip boundary condition ensures that turbulence velocity fluctuations vanish. Thus, at the wall, diffusive transport of heat and momentum in the fluid is described by the laws applicable to laminar flow. Indeed, because the turbulent shear stress and, often, the turbulent heat flux can, by continuity, increase only as the cube of the distance from the wall, there is a thin but very important sublayer immediately adjacent to the solid surface where the transport of heat and momentum is primarily by molecular diffusion. As one moves farther from the wall, again by virtue of the cubic variation, there is a rapid changeover to a state where turbulent transport dominates, a condition that normally prevails over the remainder of the flow. This thin sublayer and adjacent transition region extending to the fully turbulent regime—which we shall term the viscosity-affected sublayer

Received 26 June 2003; accepted 12 September 2003.
This work has been funded by the Engineering and Physical Sciences Research Council, through the ROPA scheme (grant reference GR/M99170), and the Models for Vehicle Aerodynamics (MOVA) EU-BRITE-EURAM Project (contract BRPR-CT98-0624).
Please note that the authors names appear in alphabetical order.
Address correspondence to S. E. Gant, Department of Mechanical, Aerospace and Manufacturing Engineering, University of Manchester Institute of Science and Technology (UMIST), PO Box 88, Manchester, M60 1QD, United Kingdom. E-mail: simon.gant@umist.ac.uk

NOMENCLATURE

a_{ij}	deviatoric and dimensionless turbulence anisotropy ($= \overline{u_i u_j}/k - 2\delta_{ij}/3$)
a_P, a_N, a_S	discretized equation coefficients at the current, north, and south subgrid nodes, respectively
c_l	equilibrium turbulence length-scale constant ($= 2.55$)
c_p	constant-pressure specific heat
c_1, c_2, c_3 c_4, c_5, c_6 $c_{\varepsilon 1}, c_{\varepsilon 2}, c_\mu$	turbulence model parameters
D	inlet pipe diameter
E	integration constant in the velocity log-law (≈ 9.79)
$\bar{E}$	integration function in the temperature log-law (a function of Prandtl number)
f_1, f_2, f_μ	turbulence model parameters
H	height from the wall surface to the pipe exit
k	turbulent kinetic energy
P	mean pressure
P_k	production rate of turbulent kinetic energy
$P_{\varepsilon 3}$	gradient production term in the low-Re model ε = equation
q_{wall}	wall heat flux
r	radius
r_b	radius of the disc
Re_ϕ	rotational Reynolds number ($= \Omega r^2/\nu$)
S	discretized equation source term
S_{ij}	mean strain-rate tensor ($= \partial U_i/\partial x_j + \partial U_j/\partial x_i$)
T	mean temperature
T^+	dimensionless mean temperature [$= (T_{\text{wall}} - T)\rho c_p U_\tau/q_{\text{wall}}$]
T^*	dimensionless mean temperature [$= (T_{\text{wall}} - T)\rho c_p k^{1/2}/q_{\text{wall}}$]
$\overline{u_i u_j}$	Reynolds stress tensor
U, V	mean Cartesian velocity components in the x and y directions, respectively
U_τ	friction velocity, defined as $U_\tau = \sqrt{\tau_{\text{wall}}/\rho}$
W	tangential velocity component ($= \Omega r$)
x, y	Cartesian coordinate axes
y	distance from the wall
y^+	dimensionless wall distance ($= U_\tau y/\nu$)
y^*	dimensionless wall distance ($= k^{1/2} y/\nu$)
Y_c	Yap correction
Γ	diffusion coefficient
δ_{ij}	Kronecker delta
ε	dissipation rate of turbulent kinetic energy
$\tilde{\varepsilon}$	isotropic part of the turbulence energy dissipation (where, by definition, $\tilde{\varepsilon} = 0$ at a wall surface)
κ	von Kármán constant in the velocity log-law (≈ 0.42)
$\tilde{\kappa}$	von Kármán constant in the temperature log-law ($= \kappa/\sigma_t$)
ν	kinematic molecular viscosity ($= \mu/\rho$)
ν_t	kinematic eddy viscosity ($= \mu_t/\rho$)
ρ	density
$\sigma_k, \sigma_\varepsilon$	empirical constants in the k and ε equations
σ_t	turbulent Prandtl number
τ_{wall}	wall shear stress
ϕ	generic variable representing $U, k, \tilde{\varepsilon}$, or T
Ω	angular velocity
Ω_{ij}	mean vorticity tensor ($= \partial U_i/\partial x_j - \partial U_j/\partial x_i$)

Subscripts

e, w, n, s	east, west, north, and south cell faces, respectively
E, W, N, S, P	east, west, north, south, and current nodal values, respectively
wall	wall value

Superscripts

$\bar{}$	mean quantity or cell-averaged value

(VASL)—is the subject of the present article. In particular, we are concerned with how one should accurately model this region in a form suitable for use in computational fluid dynamics (CFD) software.

However, accuracy is not the only criterion. The VASL, as implied above, is a region where effective transport properties change at a rate typically two or more

orders of magnitude faster than elsewhere in the flow. To resolve these changes accurately, a very fine computational mesh is required. Consequently, while the VASL occupies no more than around 1% of the flow, just resolving that region requires between 3 and 300 times as much computing time (depending on the flow problem, the complexity of the turbulence model, and the type of CFD solver adopted) as would be required if the mesh density could be kept comparable with that in the fully turbulent part of the flow. Despite this inevitably high computational cost, a great deal of work in academic circles over the last 40 years has gone into developing models of turbulence that are applicable in both the fully turbulent regime and the viscous sublayer—so-called low-Reynolds-number models. Models of this type range from the simple mixing-length schemes from the 1960s and two-equation eddy-viscosity models (EVMs) from the 1970s through to more intricate connections between the turbulent fluxes and the mean-field gradients, exemplified by non-linear eddy-viscosity models (NLEVMs) and second-moment closures.

While models of this type have enabled accurate CFD computations to be made of a range of difficult flows, they are not the subject of this article (though results obtained with such models will be included in some of the later comparisons). Instead, attention is directed at much simpler approaches for handling the sublayer region, known as "wall functions" [1]. The aim of wall functions is to replace the difference equations solved on a very fine grid across the sublayer by algebraic formulae or other low-cost routes that provide the overall resistance of the region to heat and momentum transport. Wall-function strategies are certainly the approach preferred by commercial CFD code vendors and their clients. However, most standard wall functions are based on empirically derived profiles of velocity, length scale, shear stress, and turbulent kinetic energy, which are applicable only in very simple near-wall flows and can lead to major errors in complex, non-equilibrium flows, where turbulence creation and destruction rates are far from in balance and transport effects on all dependent variables may be substantial.

Before we begin a brief review of standard wall functions, it is worth describing what is required from them in terms of their numerical implementation. First, the wall function provides an expression or value for the wall shear stress, τ_{wall}. This is employed as a source term within the discretized wall-parallel momentum equation in the computational near-wall cell and accounts for the drag on the fluid within that cell due to the wall's presence. Second, it is necessary to modify the modeled equations for the transport of turbulence within the near-wall cell to account for both viscous effects and the preferential damping of wall-normal fluctuations as the wall is approached. These changes are accounted for differently in different wall functions, sometimes by simply specifying the value of the turbulence parameter (typically k or ε) at the node adjacent to the wall, or by modifying source terms within their transport equations. Finally, for the thermal field, the wall function provides either the wall temperature, T_{wall}, or the heat flux to/from the wall, q_{wall}, which is employed in the source term of the discretized temperature equation.

The "universal" log-laws adopted by most standard wall functions for the velocity and temperature are as follows:

$$U^+ = \frac{1}{\kappa}\ln(Ey^+) \tag{1}$$

$$T^+ = \frac{1}{\tilde{\kappa}} \ln(\tilde{E} y^+) \tag{2}$$

where U^+ is the wall-parallel velocity made dimensionless by the "friction" velocity $U_\tau = \sqrt{\tau_{\text{wall}}/\rho}$, the temperature difference is made dimensionless using $T^+ = (T_{\text{wall}} - T)\rho c_p U_\tau / q_{\text{wall}}$, and y^+ is the dimensionless distance from the wall, $U_\tau y/\nu$. In addition to the above expressions, the most basic wall function specifies values of the turbulence parameters at the near-wall node assuming the turbulence to be in a state of local equilibrium. During the 1970s and 1980s, a number of modifications to this treatment were suggested, to improve its performance in non-equilibrium flows. One of the first improvements, proposed by Spalding (see Launder and Spalding [2]), was to replace the wall shear stress, τ_{wall}, in the velocity log-law with the turbulent kinetic energy, k. [Scaling the velocity with $k^{1/2}$, instead of the "friction velocity", $(\tau_{\text{wall}}/\rho)^{1/2}$, is crucial in flows involving separation, stagnation, and reattachment, where the wall shear stress vanishes.] The turbulent kinetic energy equation in the near-wall cell was solved with cell-averaged generation and dissipation rates, assuming constant shear stress and linear turbulence length-scale variation $k^{3/2}/\varepsilon \propto y$) across the near-wall cell. Chieng and Launder [3] proposed a wall function in which the near-wall cell was divided into two layers: the viscous sublayer and the fully turbulent region. In the viscous sublayer the shear stress, $\rho\overline{uv}$, was assumed to be zero and the turbulent kinetic energy to vary quadratically with wall distance, while in the fully turbulent region both $\rho\overline{uv}$ and k were assumed to vary linearly. Since, at the wall, the dissipation rate is given by $\varepsilon = 2\nu(\partial k^{1/2}/\partial y)^2)$ and k varies quadratically, ε was assumed to take a uniform value in the viscous sublayer. In the fully turbulent region, ε was obtained from assuming an equilibrium turbulence length-scale variation, $k^{3/2}/\varepsilon = c_l y$. The k equation was solved in the near-wall cell using cell-averaged production and dissipation rates. Johnson and Launder [4] modified this treatment by introducing a variable viscous sublayer thickness caused by changes in the near-wall shear stress distribution. More recently, Ciofalo and Collins [5] proposed making the sublayer thickness a function of the local turbulence intensity. Two wall functions were proposed by Amano [6]. In the first, similar assumptions were adopted to those of the earlier treatments, but instead of prescribing the nodal value of ε based on local-equilibrium assumptions, Amano suggested solving transport equations for both k and ε in the near-wall cell using cell-averaged source and sink terms. The second wall function proposed by Amano used a three-layer model, in which different profiles for k and shear stress were used in the viscous sublayer, buffer layer, and fully turbulent region. A recent proposal by Grotjans and Menter [7] assumed that the location of the wall, as specified by the user, was treated as the edge of the viscous sublayer to enable unlimited near-wall grid refinement.

All the above treatments rely on an assumed semi-logarithmic velocity and temperature distribution in the near-wall cell. In an effort to move away from these restrictions, in the mid-1980s, attempts were made at slimming down the storage requirement and computational cost of the low-Reynolds-number modeling approach by assuming a constant static pressure distribution in a thin layer adjacent to the wall—the parabolic sublayer (PSL) [8]. In this treatment, the pressure-correction algorithm was not solved in the near-wall cells and the wall-normal velocity was instead obtained directly from continuity, reducing the storage requirement and

improving the convergence rate. The PSL approach, however, encountered difficulties in complex geometries with the calculation of velocity in corner cells and was abandoned by its originators as computing power grew to enable at least some three-dimensional flows to be tackled with the low-Reynolds-number approach.

However, the growth in computational capacity has by no means removed the need for better wall functions in the applied CFD area. It has simply brought more flow problems into range that were hitherto beyond CFD's consideration. Accordingly, efforts at UMIST have recently been focused on finding accurate and efficient alternatives to standard log-law-based wall functions. Two new treatments have been developed. The first of these is based on the analytical integration of the momentum and energy equations, accounting for the effects of convection, pressure gradient, and buoyancy forces [9]. Inevitably, fairly simple prescriptions of turbulent viscosity had to be made to allow an analytical integration. The second, described in this article, is based on the efficient one-dimensional numerical integration of simplified low-Re model equations in the near-wall cell. This new numerical wall function is called UMIST-*N*: *U*nified *M*odelling through *I*ntegrated *S*ublayer *T*ransport—a *N*umerical approach.

Section 2 explains the assumptions adopted and some implementation issues associated with the numerical wall function. In Section 3, results are presented from applying the new wall function to a fully developed channel flow, using a 2-D elliptic flow solver, an axisymmetric impinging jet, and a spinning "free" disc flow. Comparisons are drawn between a standard wall function, the new wall function, and low-Re model predictions. Computational costs of these various treatments are also presented.

2. SUBGRID-BASED WALL FUNCTION: UMIST-*N*

The new UMIST-*N* wall function employs two grids: a *primary grid* equivalent to that used with standard high-Re models and conventional wall functions (with a large near-wall cell); and a *wall-function grid* which is used to calculate source terms similar to those approximated in standard treatments (such as the wall shear stress, τ_{wall}, the average turbulence energy production, $\overline{P}_k$, and average dissipation, $\overline{\varepsilon}$, over the cell). The essential difference from earlier approaches is that instead of assuming profiles of velocity and length scale, the profiles of the mean flow and turbulence parameters across this near-wall control volume are obtained from solving simplified boundary-layer-type transport equations using the fine wall-function grid. As with conventional low-Reynolds-number treatments, the turbulence model within this inner grid may be the same as, simpler than, or, in principle, more complex than that used in the outer part of the flow. In the examinations made here, we simply adopt the same underlying turbulence model in both the primary grid and the wall-function grid.

The new wall function differs from standard low-Re treatments in that it decouples the numerical solution of the near-wall region from that of the main region of the flow domain and also because it does not involve the solution of the pressure-correction equation over the subgrid. Boundary-layer equations are solved only in one dimension across the subgrid for each near-wall control volume along the wall. Due to these features, the new wall function does not suffer from the slow convergence problems of a low-Re calculation.

Calculations presented in this article were undertaken using the finite-volume elliptic code, TEAM [10], which employs a structured, fully staggered, two-dimensional Cartesian grid. In this code, scalar quantities (including pressure) are stored at main-grid nodes in the center of cells and velocities at cell faces. While the UMIST-N wall function has been developed and applied to the flows considered in this article using this fairly simple grid arrangement, the wall function can equally be applied in more complex situations (for an example of its application to three-dimensional body-fitted grids, see Gant [11]).

Governing Equations

A number of assumptions are applied within the subgrid to obtain a simplified set of transport equations: only the momentum equation(s) parallel to the wall are solved, the diffusion parallel to the wall is assumed to be negligible in comparison to that normal to the wall, and the pressure gradient is assumed to be constant across all the near-wall subgrid cells. For illustration, the simplified low-Re transport equations solved over the subgrid are shown below in Cartesian coordinates for the case where the flow is two-dimensional with just two components of velocity, where y is the wall-normal direction.

Wall-parallel U-momentum:

$$\rho U\frac{\partial U}{\partial x}+\rho V\frac{\partial U}{\partial y}=-\frac{\mathrm{d}P}{\mathrm{d}x}+\frac{\partial}{\partial y}\left(\mu\frac{\partial U}{\partial y}-\rho\overline{uv}\right) \tag{3}$$

Turbulent kinetic energy, k:

$$\rho U\frac{\partial k}{\partial x}+\rho V\frac{\partial k}{\partial y}=\frac{\partial}{\partial y}\left[\left(\mu+\frac{\mu_t}{\sigma_k}\right)\frac{\partial k}{\partial y}\right]+P_k-\rho\varepsilon \tag{4}$$

Dissipation rate, $\tilde{\varepsilon}$:

$$\rho U\frac{\partial \tilde{\varepsilon}}{\partial x}+\rho V\frac{\partial \tilde{\varepsilon}}{\partial y}=\frac{\partial}{\partial y}\left[\left(\mu+\frac{\mu_t}{\sigma_\varepsilon}\right)\frac{\partial \tilde{\varepsilon}}{\partial y}\right]+c_{\varepsilon 1}f_1P_k\frac{\tilde{\varepsilon}}{k}-c_{\varepsilon 2}f_2\rho\frac{\tilde{\varepsilon}^2}{k}+P_{\varepsilon 3}+\rho Y_c \tag{5}$$

Temperature, T:

$$\rho U\frac{\partial T}{\partial x}+\rho V\frac{\partial T}{\partial y}=\frac{\partial}{\partial y}\left[\left(\frac{\mu}{\sigma}+\frac{\mu_t}{\sigma_t}\right)\frac{\partial T}{\partial y}\right] \tag{6}$$

In the absence of buoyancy or other fluctuating force fields, the production rate of turbulent kinetic energy, P_k, is given by

$$P_k=-\rho\overline{uv}\left(\frac{\partial U}{\partial y}+\frac{\partial V}{\partial x}\right)-\rho\overline{u^2}\frac{\partial U}{\partial x}-\rho\overline{v^2}\frac{\partial V}{\partial y} \tag{7}$$

where the terms $P_{\varepsilon 3}$ and Y_c and the damping functions f_1 and f_2 are those associated with the particular low-Re model being used, and σ_t is taken as 0.9.

In the present work, the subgrid wall function has been tested with both the linear k–ε model of Launder and Sharma [12] and the cubic nonlinear eddy-viscosity model (NLEVM) of Craft et al. [13, 14], although, in principle, any turbulence closure can be used. In the former model, the Reynolds shear stress, $\rho\overline{uv}$, is determined from

$$\rho\overline{uv} = -\mu_t\left(\frac{\partial U}{\partial y} + \frac{\partial V}{\partial x}\right) \tag{8}$$

where the eddy viscosity is given by

$$\mu_t = c_\mu f_\mu \frac{k^2}{\tilde{\varepsilon}} \tag{9}$$

In the two-equation NLEVM, additional quadratic and cubic functions of the strain rate and vorticity are introduced in the anisotropy tensor, as follows:

$$\begin{aligned} a_{ij} \equiv \frac{\overline{u_i u_j}}{k} - \frac{2}{3}\delta_{ij} = &-\frac{\nu_t}{k}S_{ij} + c_1\frac{\nu_t}{\tilde{\varepsilon}}\left(S_{ik}S_{kj} - \frac{1}{3}S_{kl}S_{kl}\delta_{ij}\right) \\ &+ c_2\frac{\nu_t}{\tilde{\varepsilon}}(\Omega_{ik}S_{kj} + \Omega_{jk}S_{ki}) + c_3\frac{\nu_t}{\tilde{\varepsilon}}\left(\Omega_{ik}\Omega_{kj} - \frac{1}{3}\Omega_{lk}\Omega_{lk}\delta_{ij}\right) \\ &+ c_4\frac{\nu_t k}{\tilde{\varepsilon}^2}(S_{ki}\Omega_{lj} + S_{kj}\Omega_{li})S_{kl} \\ &+ c_5\frac{\nu_t k}{\tilde{\varepsilon}^2}\left(\Omega_{il}\Omega_{lm}S_{mj} + S_{il}\Omega_{lm}\Omega_{mj} - \frac{2}{3}S_{lm}\Omega_{mn}\Omega_{nl}\delta_{ij}\right) \\ &+ c_6\frac{\nu_t k}{\tilde{\varepsilon}^2}S_{ij}S_{kl}S_{kl} + c_7\frac{\nu_t k}{\tilde{\varepsilon}^2}S_{ij}\Omega_{kl}\Omega_{kl} \end{aligned} \tag{10}$$

where the strain-rate and vorticity tensors are given by

$$S_{ij} = \frac{\partial U_i}{\partial x_j} + \frac{\partial U_j}{\partial x_i} \qquad \Omega_{ij} = \frac{\partial U_i}{\partial x_j} - \frac{\partial U_j}{\partial x_i} \tag{11}$$

In addition to the above non-linear constitutive relation, the NLEVM also takes c_μ to be a function of invariants of the strain and vorticity tensors. The model has previously been found to perform well in a wide variety of flows, including impinging jets and abrupt pipe expansions [14], flow in straight and curved channels, in rotating pipes, and over a turbine blade cascade [15], flow through a square-sectioned U-bend, a plane diffuser, and around a square cylinder near a wall [16].

Implementation of the UMIST-*N* Wall Function

The near-wall cell of the primary grid is divided into a number of subgrid cells which increase in size with distance from the wall according to a simple geometric expansion (see Figure 1*a*). To establish a grid-independent solution, the number and distribution of the subgrid cells needs to be adjusted for each case studied (this can be assessed independently of the grid dependence of the primary grid, by freezing the values of the primary grid quantities and solving only the wall-function transport equations). Experience has shown that the UMIST-*N* wall function is far less sensitive to the size of the near-wall primary-grid cell than log-law-based wall functions. In cases where the Prandtl number is larger than unity, the number of subgrid cells can simply be increased to resolve the thinner thermal sublayer. Although this will increase the computing time slightly, one would expect a full low-Reynolds-number model treatment of the same flow to incur a far greater increase in computing time.

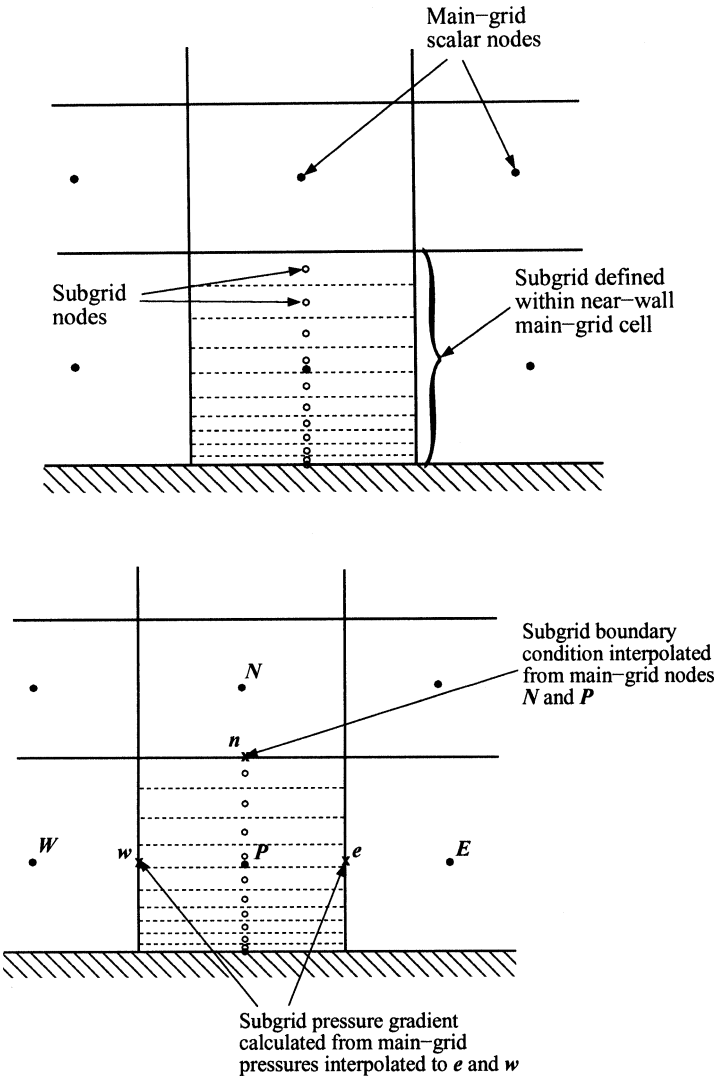

Figure 1. (Top) Subgrid arrangement within the near-wall main-grid control volume. (Bottom) Subgrid boundary conditions and pressure gradient.

Subgrid convection is modeled in non-conservative form, as shown above [Eqs. (3)–(6)] since, in an isothermal situation where there is no wall heating, the conservative form of the convection term can lead to a non-zero source/sink term in the subgrid temperature equation, due to mass flux imbalance through the cell faces. Convection parallel to the wall is calculated using neighboring subgrid values. The wall-normal V-velocity (required to evaluate the wall-normal convection) is calculated from subgrid continuity and is then scaled to ensure that the subgrid velocity at the outer boundary (shown as position n in Figure 1*b*) matches the main-grid velocity at that location. Although continuity is not rigorously satisfied in the

subgrid cells due to this scaling, it is necessary to ensure consistent velocity boundary conditions. Subgrid convective terms are discretized using an upwind scheme. In order to calculate gradients parallel to the wall, to find the V velocity, and to provide initial conditions for the subgrid calculation, it is necessary to store each of the subgrid profiles along the wall. The alternative approach of not storing each subgrid profile was investigated but was found to cause some numerical instability due to the less accurate wall-parallel convection treatment which was necessary and also led to prolonged computing times, since several iterations of the subgrid calculation were required per main-grid iteration (for details, see Gant [11]).

The pressure gradient (dP/dx) is calculated from the interpolated main-grid pressure values at locations e and w (see Figure 1*b*), and its value is assumed to apply across the near-wall cell. Boundary conditions at the wall are the same as those used in low-Re calculations. The boundary conditions at the northern boundary are determined from linear interpolation of main-grid nodal values at N and P.

Coding of the subgrid transport equations is relatively straightforward, with each equation integrated and discretized using the finite-volume method as in simple one-dimensional diffusion problems (see, for instance, Versteeg and Malalasekera [17]). The subgrid transport equations can be written in the general form

$$\rho U\frac{\partial\phi}{\partial x}+\rho V\frac{\partial\phi}{\partial y}=\frac{\partial}{\partial y}\left(\Gamma\frac{\partial\phi}{\partial y}\right)+S \tag{12}$$

where ϕ denotes U, k, ε, or T. Integration of this equation across a subgrid cell and rearranging it in terms of coefficients of subgrid nodal values leads to the following discretized equation:

$$a_P\phi_P=a_N\phi_N+a_S\phi_S+S \tag{13}$$

The source term, S, can be expressed as

$$S=s_P\phi_P+s_U \tag{14}$$

Following conventional practice, to improve stability, negative sources in the subgrid k and $\tilde{\varepsilon}$ equations are included in source s_P, which can be incorporated into the left-hand side of Eq. (13) to increase the diagonal dominance of the coefficient matrix. All other sources, including the wall-parallel pressure gradient in the momentum equation, are included in s_U. In a similar manner, terms resulting from convection parallel to the wall are split between sources s_U and s_P depending on their sign. Convection normal to the wall is treated implicitly and results in additional terms in s_P, a_N, and a_S. A small amount of under-relaxation is required for the subgrid k and $\tilde{\varepsilon}$ equations (with typical under-relaxation factors of 0.9), while the subgrid momentum and temperature equations require no under-relaxation. The discretized subgrid transport equations are solved using a tri-diagonal matrix algorithm (TDMA). Only one sweep of the subgrid TDMA is performed for each main-grid iteration, so the subgrid solution converges as the main-grid solution converges (it is not necessary to fully converge the subgrid solution for each main-grid iteration).

Following each subgrid iteration, wall-function parameters are calculated: wall shear stress, volume-averaged source and sink terms in the k and $\tilde{\varepsilon}$ equations

($\overline{P_k}, \overline{\varepsilon}, \overline{P_k\tilde{\varepsilon}/k}, \overline{f_2\tilde{\varepsilon}^2/k}, \overline{P_{\varepsilon 3}}$, and $\overline{Y_c}$), and wall temperature, T_{wall}, or wall heat flux, q_{wall}. These wall-function parameters are then applied as source terms in the main-grid wall-adjacent cells following the conventional wall-function approach. Low-Reynolds-number terms are included in the equations solved in the main grid so that, in a stagnant flow region where turbulent Reynolds numbers are locally small even in the primary grid, the turbulence model is still able to cope.

3. WALL FUNCTION APPLICATIONS

Channel Flow

The new wall function was developed by reference to a simple 2-D fully developed channel flow with periodic inlet and outlet boundaries and Reynolds number, based on bulk velocity and channel width (wall to wall), of 100,000. The results obtained using two different near-wall main-grid cell sizes are shown in Figure 2, corresponding to near-wall nodal y^+ values of approximately 50 and 100, and compared with a conventional low-Re approach. Both UMIST-*N* wall function and low-Re results were obtained using the model of [12]. The wall-function results are in good agreement with the low-Re model predictions for both near-wall cell sizes. A small discrepancy in the near-wall main-grid turbulent kinetic energy is due to the linear interpolation between the two near-wall nodes used to obtain the subgrid boundary condition several other methods of interpolating have been tested for the subgrid boundary condition, but none provided any significant improvements without diminishing the generality of the wall function. The results also show little dependence on the size of the near-wall main-grid cell.

Axisymmetric Impinging Jet

There have been several previous numerical simulations and experimental studies of the impinging jet, reflecting the range of related industrial flows and the usefulness of this particular geometry for testing turbulence models. Jet impingement causes high levels of heat transfer rates near the stagnation point and is used in

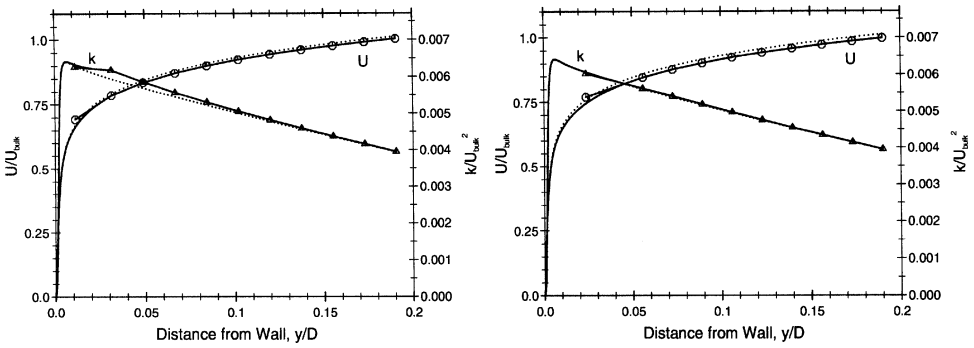

Figure 2. Mean velocity and turbulent kinetic energy profiles in the channel flow at Re = 100,000 using two different grids with $y^+ \approx 50$ (left) and $y^+ \approx 100$ (right); dotted lines, low-Re model results; solid-lines, UMIST-*N* wall function results (where symbols indicate the primary grid nodal values and the solid line without symbols represents the solution across the subgrid).

industrial applications where heating, cooling, or drying processes are required. As a test case, the impinging jet offers insight into the behavior of turbulence models in flow regimes far removed from the traditional simple shear flow, since there is significant irrotational straining near the stagnation point, and near the edge of the impinging jet there is strong streamline curvature. Moving farther downstream, the flow tends toward a radial wall jet in which the maximum shear stress occurs outside the wall region. Turbulence models and wall functions are often developed with reference to flows parallel to walls where none of these features occur.

In the present study, predictions obtained using the UMIST-N wall function are compared with those obtained from the Chieng and Launder wall function (hereafter, CLWF) and low-Reynolds-number model results, using the linear k–ε model of [12] and the non-linear k–ε model of Craft et al. [14]. The CLWF was chosen for comparison following a study which showed that it outperformed other simple wall functions in impinging flows [18], in agreement with an earlier study by Amano and Jensen [19].

The impinging jet geometry studied here is one of those examined experimentally by Baughn et al. [20]. and Cooper et al. [21] with a jet discharge height-to-diameter ratio, $H/D = 4$, and Reynolds number, based on the inlet pipe diameter and bulk velocity, of 70,000. The flow domain dimensions and boundary conditions are shown in Figure 3. A short length of pipe (half a jet diameter in length) was included within the computational domain to avoid numerical instability arising from the boundary between the jet exit and the entrainment boundary. A fully developed pipe flow was applied at the entrance to the pipe (i.e., 4.5 jet diameters from the impingement wall).

For the low-Reynolds-number model a grid of 90×70 (axial $\times$ radial) nodes was used in which cells were strongly clustered toward the wall. The wall-function grids used in this study had an identical distribution of nodes to the low-Re grid in the radial direction. In the axial direction, 45 nodes were used, with some clustering toward the wall and near the pipe entrance. To determine the effects of changing the near-wall cell size, four different near-wall cell sizes were tested, corresponding to y^*

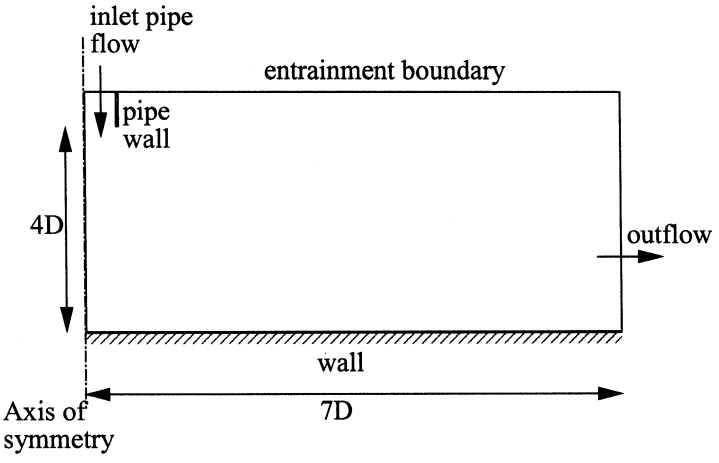

Figure 3. Impinging jet flow domain and boundary conditions.

values varying in the range $310 \leq y^* \leq 620$ at the stagnation point and $60 \leq y^* \leq 150$ at $r/D = 6$. In the Nusselt number comparisons given later (Figures 4 and 5), these four cell sizes are denoted by $DX = 250$, 300, 400, and 500. The actual value of DX represents the ratio of the physical width of the near-wall main-grid cell (in the wall-normal direction) to that used in the low-Reynolds-number grid.

The UMIST-N wall function applied to the impinging jet was identical to the illustrative form in Section 2 with the exception that axisymmetric terms were included in the transport equations. Care was taken to ensure that the subgrid wall-function predictions were independent of the subgrid node density. Typically this involved 40 subgrid nodes with an algebraic expansion ratio of 1.08. The Chieng and Launder wall function [3] was of the same form as that described in Section 1 with, in addition, contributions from the normal stresses in the cell-averaged production rate, $\overline{P_k}$. In both the low-Re and high-Re computations, convective transport of momentum and temperature was approximated using the third-order quadratic upwind scheme, QUICK [22], while power-law differencing, PLDS [23], was used for turbulence parameters.

As is now well known, linear EVMs lead to a spurious generation of k through the normal straining associated with stagnation. That is why the low-Re k–ε model leads to Nusselt numbers at the stagnation point more than twice as high as the measurements (see Figure 4). The UMIST-N wall function captures the full low-Reynolds-number model behavior accurately (Figure 4b). While standard wall functions produce much lower heat transfer coefficients, closer to the measured values, this apparent success is a consequence of partly cancelling errors. To mimic reliably the effects of a stagnation strain field, one must adopt a more comprehensive link between the deformation and stress tensors. The cubic eddy-viscosity model of Craft et al. [14] goes some way toward this (Figure 5). When used with conventional wall functions (Figure 5a), rather poor agreement is obtained with a stagnation point Nusselt number 30% below the low-Re model and a significant sensitivity to the size of the near-wall cell for $1.3 < r/D < 2.5$. In contrast, the UMIST-N wall function mimics the low-Re behavior closely, with little dependency on the size of the wall-adjacent cell of the primary grid (Figure 5b).

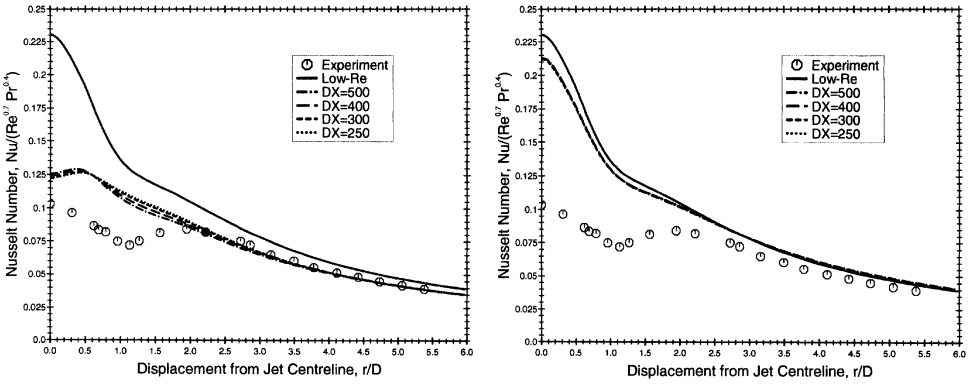

Figure 4. Nusselt number predictions for the impinging jet ($H/D = 4, \mathrm{Re} = 70,000$) using the linear k–ε model; broken lines are wall function results with different near-wall cell sizes; (left) Chieng and Launder wall function; (right) UMIST-N wall function.

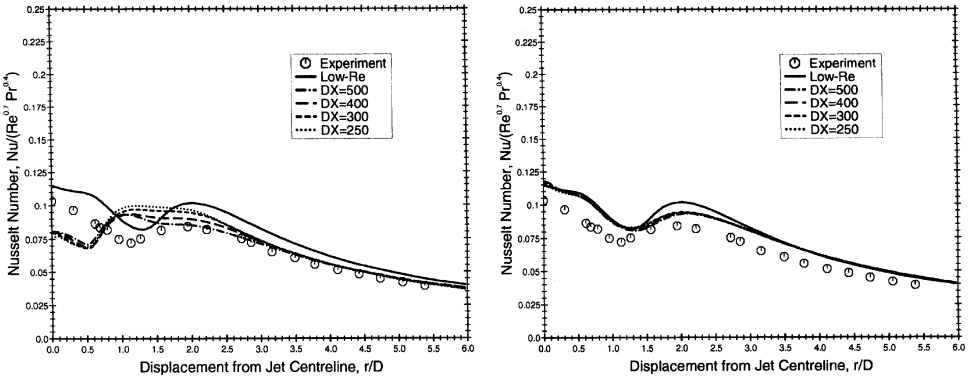

Figure 5. Nusselt number predictions for the impinging jet ($H/D = 4, \mathrm{Re} = 70,000$) using the nonlinear k–ε model; broken lines are wall-function results with different near-wall cell sizes; (left) Chieng and Launder wall function; (right) UMIST-N wall function.

Semi-logarithmic plots of the normalized temperature at two radial locations ($r/D = 0.5$ and 4.0) show the difference between the CLWF and the UMIST-N wall functions more clearly. At $r/D = 0.5$ (Figure 6*a*), the radial velocity is undergoing strong acceleration and the log-law is clearly inapplicable. Indeed, the near-wall dimensionless temperature, T^*, at the near-wall node predicted by the CLWF is nearly twice that predicted by the low-Re model. The agreement between log-law wall function and the low-Re model improves farther downstream (Figure 6*b*), although the slope of the log-law is in poor agreement with that of the low-Re model. The UMIST-N wall-function predictions are in close agreement with the low-Re results, with a difference of only a few percent, at both radial locations. (Note that in Figures 6*a* and 6*b* the primary-grid nodal values, marked by circles, are joined together by straight, solid lines. The subgrid distribution is also shown by a solid line, therefore creating an overlap of solid lines within the near-wall cell. The end of

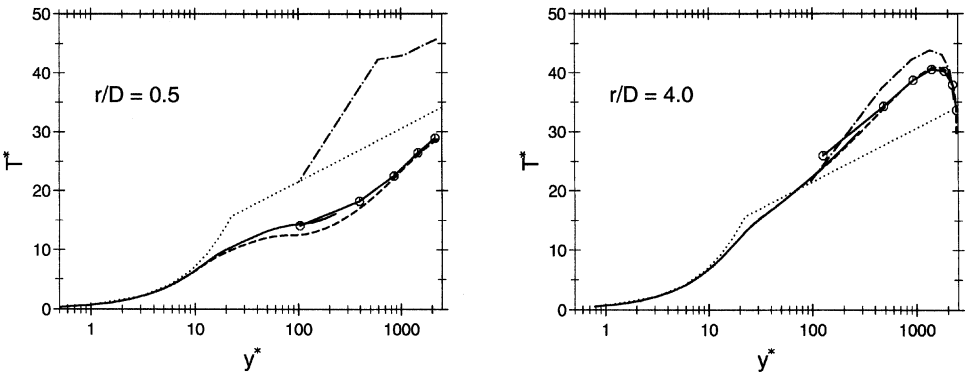

Figure 6. Dimensionless temperature profiles in the impinging jet flow ($H/D = 4, \mathrm{Re} = 70,000$) using the nonlinear k–ε model at two radial locations: (left) $r/D = 0.5$; (right) $\tau./D = 4.0$. —○—, UMIST-N wall function (circles indicate the position of primary grid nodes and the solid line without symbols represents the solution across the subgrid); – – –, low-Re model; —·—, Chieng and Launder wall function; ···, "universal" log-law.

the line representing the subgrid distribution does not intersect the straight line joining the two primary grid nodes nearest to the wall because the x-axis scale is logarithmic. Joining two points with a straight line on these axes is equivalent to a logarithmic interpolation, whereas the subgrid boundary condition is calculated from a linear interpolation of the two nodal values. If one was to plot the same profiles on linear axes, the two lines would intersect at the subgrid boundary—for example, see Figure 2.)

Table 1 compares the CPU costs for the axisymmetric impinging-jet computations using the nonlinear k–ε model. Calculations were run on a Silicon Graphics O_2 workstation with the same levels of under-relaxation and compiler optimization in each case. The tables show that the new wall function requires up to 60% more computing time than a standard wall function. This is a small price to pay in return for the much greater accuracy of the prediction. Indeed, the predictions are very similar to those returned by the low-Reynolds-number NLEVM, but the computing time required is less than one-eighth of the latter treatment.

Spinning "Free" Disc Flow

In the free-disc flow, the disc of radius r_b rotates with angular velocity Ω and, due to the no-slip condition on the surface of the spinning disc, a tangential velocity ($W = \Omega r$) is imparted to the fluid in contact with the disc. A radial outflow of fluid from the center of the disc is also induced by the centrifugal force. At sufficiently high rotational speeds and at a sufficient distance from the disc axis, the boundary layer becomes turbulent. Once the boundary layer has become fully turbulent, the tangential velocity exhibits a logarithmic velocity profile near the wall, while the radial velocity increases from zero at the wall to a peak and then decays with distance from the disc. The large near-wall cells commonly used with wall functions cover the region of the flow where the peak in the radial velocity profile occurs. Capturing the skewing of the velocity vector across the near-wall cell using wall functions based on the log-law velocity profile is therefore an impossible task, since it is assumed that the wall shear stress acts in the same direction as the velocity vector at the near-wall node.

The performance of the new UMIST-N wall function is compared in the free-disc flow to that of the CLWF and a low-Reynolds-number treatment using the linear k–ε model [12]. The CLWF switched from using a logarithmic profile for both the radial and tangential velocity to a linear profile if the dimensionless wall distance, $y^* = k^{1/2}y/\nu$, fell below 21.2.

Table 1. Computing times for the axisymmetric impinging jet using the Craft et al. NLEVM

	Wall functions		
	Chieng and Launder	UMIST-N	Low-Re, Craft et al.
Number of nodes	70×45	70×45 (+ 40)	70×90
CPU time per iteration (s)	0.158	0.260	0.324
No. of iterations	1,426	1,380	9,116
Total CPU time (s)	226	359	2,955
Relative CPU time	1	1.59	13.08

Figure 7 shows the domain size and boundary conditions used for the free-disc study. The Reynolds number at the outside edge of the disc is $\mathrm{Re}_\phi = 3.3 \times 10^6$. Following a grid-refinement study, a grid of 70×120 (axial $\times$ radial) nodes was used for the low-Reynolds-number model. Four different grids were used for the wall-function calculations, with the same distribution of nodes in the radial direction as the low-Re model but between 22 and 30 nodes in the wall-normal direction (for the near-wall node at the outside edge of the disc, y^* was around 130 with the 30×120 grid and around 550 for the 22×120 grid); for the 22×120 grid, nodes were uniformly distributed across the domain in the axial direction, whereas the other grids all involved some clustering of cells toward the wall.

The QUICK scheme was used to approximate convective terms in the momentum and temperature equations, while PLDS was used for turbulence parameters. A constant wall temperature condition was imposed on the wall to conform with the experimental heat transfer measurements of Cobb and Saunders [24]. The UMIST-*N* wall function solved transport equations across the near-wall cell for both radial and tangential velocity components, turbulence parameters (k and $\tilde{\varepsilon}$), and temperature. As before, the arrangement of subgrid nodes within the near-wall cell was adjusted to ensure that a grid-independent solution was obtained. This involved 30 subgrid nodes with an algebraic expansion ratio of 1.10 for the 28×120 grid. The flow field was initialized with a uniform turbulence level and, as the calculation progressed, turbulence decayed near the axis of the disc to form a laminar boundary layer, while at greater radial distances the flow remained fully turbulent. Some care was needed with both the low-Reynolds-number models and the UMIST-*N* wall function to obtain results which were independent of the initial turbulence level (for details, see Gant [11]. Calculations were continued until all the residuals decreased by at least three orders of magnitude from their maximum values. It was verified that using more stringent convergence criteria did not affect the results.

Figures 8*a* and 8*b* show the predicted integral Nusselt number for the spinning-disc flow using the CLWF and the UMIST-*N* wall functions. The Nusselt number predicted with the former wall function is sensitive to the size of the near-wall cell, largely as a result of the switch used to select laminar or turbulent wall functions depending on the value of y^*. In contrast, the UMIST-*N* wall function shows good overall agreement with the Nusselt number predicted by the low-Re model.

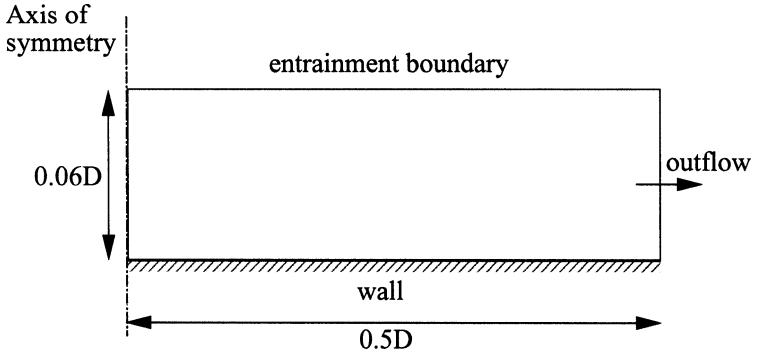

Figure 7. Spinning "free" disc flow boundary conditions.

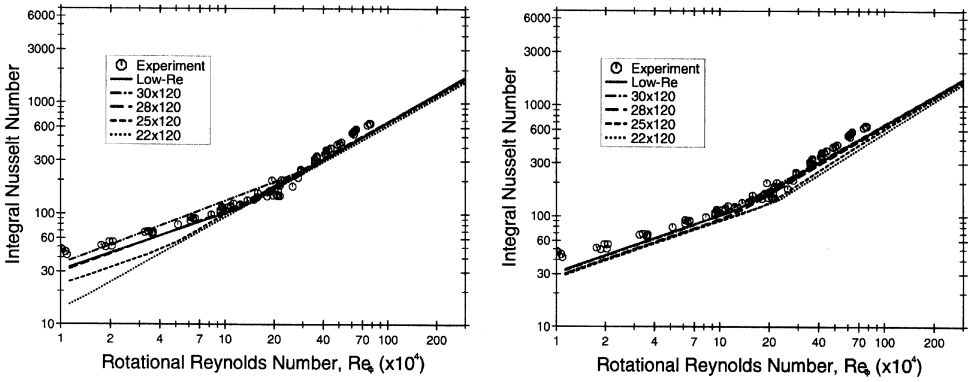

Figure 8. Predicted integral Nusselt number in the free-disc flow using the linear $k - \varepsilon$ model with: (left) Chieng and Launder wall function; (right) UMIST-*N* wall function. Solid line, low-Re model; broken lines, wall function results for different grid arrangements; ○, experimental values from Cobb and Saunders [24].

The slope of the Nu profile in the laminar and turbulent regions of the flow is close to that observed with the low-Re model, although there is some sensitivity to the size of the near-wall cell in the predicted transition location.

Figures 9*a* and 9*b* show the radial and tangential velocity profiles at $\mathrm{Re}_\phi = 1.0 \times 10^6$ on wall–law axes. The tangential velocity profile calculated by the CLWF is in fairly good agreement with the low-Re model. This behavior is to be expected, since the tangential velocity exhibits a logarithmic profile near the wall. The radial velocity profile, however, is less well predicted. This scheme calculates the radial velocity at the near-wall node from the "universal" log-law (as shown by Figure 9, where the dotted line intersects the chain line of the log-law). This is clearly in poor agreement with the radial velocity profile from the low-Re model. Both the radial and tangential velocity profiles using the UMIST-*N* wall function profiles are,

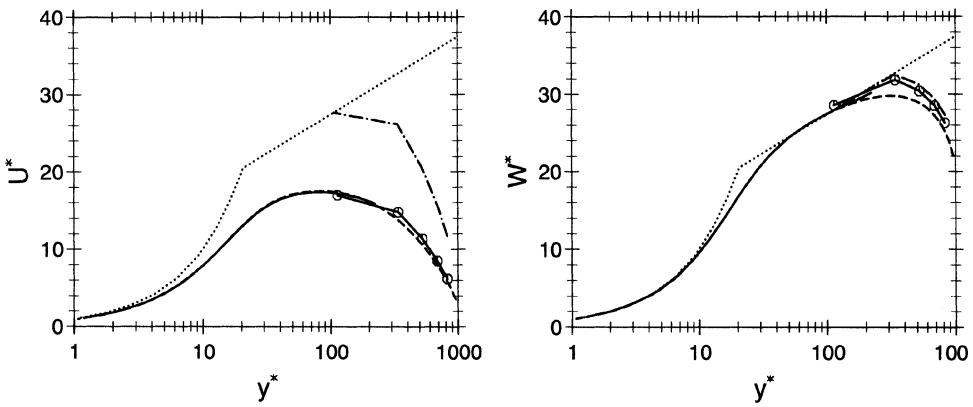

Figure 9. Velocity profiles for the free-disc flow at $\mathrm{Re}_\phi = 1.0 \times 10^6$ using wall-law axes; (left) radial *U*-velocity and (right) tangential *W*-velocity; –○–, UMIST-*N* wall function (circles indicate the position of primary grid nodes and the solid line without symbols represents the solution across the subgrid); – – –, low-Re model; – · –, Chieng and Launder wall function; · · ·, "universal" log-law.

Table 2. Computing times for the free-disc ($Re_\phi = 3.3 \times 10^6$) with the linear k–ε model

	Wall functions		
	Chieng and Launder	UMIST-N	Low-Re, Launder-Sharma
Number of nodes	120×28	120×28 (+30)	120×70
CPU time per iteration (s)	0.07	0.14	0.20
No. of iterations	2,208	2,363	19,928
Total CPU time (s)	154	339	3,996
Relative CPU time	1	2.2	29.4

however, in excellent agreement with the low-Re model. In particular, the velocity profiles across the near-wall cell predicted by the UMIST-N wall function are almost a perfect match to the low-Re model profiles.

Computing times for the spinning-disc flow are shown in Table 2. The same under-relaxation factors were used in the two wall function calculations and the low-Re model. Calculations were performed on a single node of a Silicon Graphics Origin 2000 computer with the same levels of compiler optimization in each case. The UMIST-N calculations took approximately twice as much CPU time as the log-law-based CLWF but were, nevertheless, more than 13 times faster than the low-Re model.

4. CONCLUDING REMARKS

The development of a new subgrid-based wall function has been presented in which boundary-layer-type transport equations are solved locally across an embedded grid within the near-wall cell. Implementation issues, such as the numerical treatment of the subgrid transport equations and the calculation of wall-normal velocity, have been discussed. Several quite complex flows near walls have been examined, including impinging jet and rotating-disc flows. It has been shown that the new wall function achieves excellent agreement with results obtained using low-Reynolds-number models, while requiring only a modest increase in computing time compared with a standard wall function. Computing times with the new approach are still an order of magnitude less than standard low-Reynolds-number treatments.

REFERENCES

1. S. V. Patankar and D. B. Spalding, *Heat and Mass Transfer in Boundary Layers*, Morgan Grampian Press, London, 1967.
2. B. E. Launder and D. B. Spalding, The Numerical Computation of Turbulent Flows, *Comput. Meth. Appl. Mech. Eng.*, vol. 3, pp 269–289, 1974.
3. C. C. Chieng and B. E. Launder, On the Calculation of Turbulent Heat Transport Downstream from an Abrupt Pipe Expansion, *Numer. Heat Transfer*, vol. 3, pp. 189–207, 1980.
4. R. W. Johnson and B. E. Launder, Discussion of "On the Calculation of Turbulent Heat Transport Downstream from an Abrupt Pipe Expansion," *Numer. Heat Transfer*, vol. 5, pp. 493–496, 1982.
5. M. Ciofalo and M. W. Collins, k–ε Predictions of Heat Transfer in Turbulent Recirculating Flows Using an Improved Wall Treatment, *Numer. Heat Transfer* B, vol. 15 pp. 21–47, 1989.

6. R. S. Amano, Development of a Turbulence Near-Wall Model and Its Application to Separated and Reattached Flows, *Numer. Heat Transfer*, vol. 7, pp. 59–75, 1984.
7. H. Grotjans and F. R. Menter, Wall Function for General Application CFD Codes, in *Computational Fluid Dynamics 1998, Proc. Fourth European CFD Conf. ECCOMAS*, Wiley, Chichester, England, 1998.
8. H. Iacovides and B. E. Launder, PSL—An Economical Approach to the Numerical Analysis of Near-Wall Elliptic Flows, *ASME J. Fluids Eng.*, vol. 106, pp. 245, 1984.
9. T. J. Craft, A. V. Gerasimov, H. Iacovides, and B. E. Launder, Progress in the Generalization of Wall-Function Treatments, *Int. J. Heat Fluid Flow*, vol. 23, pp. 148–160, 2002.
10. P. G. Huang and M. A. Leschziner, TEAM, an Introduction and Guide to the Computer Code, University of Manchester, Manchester, UK, 1984.
11. S. E. Gant, Development and Application of a New Wall Funtion for Complex Turbulent Flows, Ph.D. thesis, University of Manchester Institute of Science and Technology, Manchester, UK, 2002.
12. B. E. Launder and B. I. Sharma, Application of the Energy-Dissipation Model of Turbulence to the Calculation of Flow near a Spinning Disc, *Lett. Heat Mass Transfer*, vol. 1, pp. 131–138, 1974.
13. T. J. Craft, B. E. Launder, and K. Suga, Development and Application of a Cubic Eddy-Viscosity Model of Turbulence, *Int. J. Heat Fluid Flow*, vol. 17, pp. 108–115, 1996.
14. T. J. Craft, H. Iacovides, and J. H. Yoon, Progress in the Use of Non-linear Two-Equation Models in the Computation of Convective Heat-Transfer in Impinging and Separated Flows, *Flow, Turbulence Combustion*, vol. 63, pp. 59–80, 1999.
15. K. Suga, Development & Application of a Non-linear Eddy Viscosity Model Sensitized to Stress and Strain Invariants, Ph.D. thesis, University of Manchester, Manchester, UK, 1995.
16. C. M. E. Robinson, Advanced CFD Modelling of Road–Vehicle Aerodynamics, Ph.D. thesis, University of Manchester Institute of Science and Technology, Manchester, UK, 2001.
17. H. K. Versteeg and W. Malalasekera, *An Introduction to Computational Fluid Dynamics*, Longman Scientific & Technical, Harlow, England, 1995.
18. S. E. Gant, Assessment of Wall Function Practices for Impinging Flows, First-Year Ph.D. Report, University of Manchester Institute of Science and Technology, Manchester, UK, 1999.
19. R. S. Amano and M. K. Jensen, Turbulent Heat Transfer of Impinging Jet on a Flat Plate, ASME Paper 82-WA/HT-55, Winter Annual Meeting, Phoenix, AZ, 1982.
20. J. W. Baughn, X. J. Yan, and M. Mesbah, The Effect of Reynolds Number on the Heat Transfer Distribution from a Flat Plate to a Turbulent Impinging Jet, ASME Winter Annual Meeting, Anaheim, California, November 1992.
21. D. Cooper, D. C. Jackson, B. E. Launder, and G. X. Liao, Impinging Jet Studies for Turbulence Model Assessment, Part 1: Flow Field Experiments, *Int. J. Heat Mass Transfer*, vol. 36, no. 10, pp. 2675–2684, 1993.
22. B. P. Leonard, A Stable and Accurate Convective Modelling Procedure Based on Quadratic Upstream Interpolation, *Comput. Meth. Appl. Mech. Eng.*, vol. 19, pp. 59–98, 1979.
23. S. V. Patankar, Numerical Heat Transfer and Fluid Flow, Hemisphere, McGraw-Hill, New York, 1980.
24. E. C. Cobb and O. A. Saunders, Heat Transfer from a Rotating Disk, *Proc. Roy. Soc. Lond. A*, vol. 236, pp. 343–351, 1956.